PAPER

Check for updates

Post-synthetic modification approach for tandem functionalization of a 2D-layered Zn-coordination polymer: from exfoliated nanosheets to a 3D supramolecular structure with enhanced dye adsorption efficiency†

Qasem Maleki, [ID] [a] Valiollah Nobakht [ID] *[b] and Sepideh Samiee [ID] [a]

Post-synthetic modification (PSM) represents a promising approach for enhancing the properties of coordination polymers (CPs) and MOFs by introducing new functional groups and tailored surface chemistry. This study details a tandem PSM of a 2D Zn-coordination polymer (parent compound), **[Zn(AIP)(DMSO)]$_n$** (**Zn-CP**), to generate various functionalized structures. In the first step of PSM, **Zn-CP-df** was created through the removal of coordinated DMSO molecules from **[Zn(AIP)(DMSO)]$_n$** to form Lewis acid sites. Subsequently, the stacked layers of **Zn-CP-df** were exfoliated to **Zn-CP-df-ex** nanosheets. In the second step, **Zn-CP-df** was reacted with ethylenediamine (en) to generate a multilayered structure of **[Zn(AIP)(en)]$_n$** (**Zn-CP-en**), decorated with Lewis-base sites. In the third PSM step, the nanosheets were functionalized with Brønsted-acid groups (−SO$_3$H moieties) *via* the reaction of **Zn-CP-en** with 1,3-propanesultone (ps) to form **[Zn(AIP)(en)(ps)]$_n$** (**Zn-CP-en-ps**). In parallel with step two, **Zn-CP-df** layers were cross-linked by 1,3-diaminopropane (dap) to form a 3D supramolecular framework, **[Zn(AIP)(dap)]$_n$** (**Zn-CP-dap**), exhibiting distinct properties compared to the **Zn-CP-en**. The structures of the functionalized compounds were characterized by FT-IR, PXRD, CHNS, zeta-potential, FESEM, and TEM analyses. The adsorption performance of all synthesized compounds was evaluated for both anionic and cationic dyes to elucidate the structure−property relationships between the post-synthetic modifications and dye adsorption efficiency.

Introduction

Two-dimensional (2D) materials with unique properties, such as exceptional surface chemistry, unusual physicochemical behavior, and quantum size effects, have attracted considerable attention in recent years.[1–3] The discovery of graphene's 2D sheet structure by Geim *et al.*[4] in 2004 spurred extensive research into related layered materials, including transition metal dichalcogenides (TMDs),[5,6] graphitic carbon nitride (g-C$_3$N$_4$),[7] silicene,[8] transition metal carbides, nitrides, and carbonitrides (MXenes),[9] as well as 2D covalent–organic frameworks (COFs),[10] and 2D coordination polymers (CPs).[11]

Coordination polymers (CPs) are crystalline structures where organic linkers are coordinated to metallic nodes or clusters, creating a highly regular framework from 1D to 3D. The bottom-up approach is one of the best methods to produce extra-thin nanosheets of 2D CPs, which are ideal for various applications such as sensing,[12,13] sorption,[14,15] storage, separation of guest molecules,[14,16,17] second-order nonlinear optical (NLO) properties,[18] luminescence,[18] catalysis,[19,20] proton and electrical conduction, and energy storage and supercapacitors.[21–25] Among the various metal ions employed in the design and synthesis of CPs, Zn(II) plays a pivotal role in coordination chemistry due to its flexible coordination geometry, d^{10} electronic configuration, and non-toxic nature, making it an excellent candidate for designing CPs with diverse structures and tunable functionalities.[26–29] However, controlling the architectures of CPs remains a challenge due to various factors affecting their assembly, such as geometry of the linker ligands, metal-to-ligand ratio,[30,31] counter anions,[32–34] guest molecules, and different chemical functional groups.[35]

[a] Department of Chemistry, Faculty of Science, Shahid Chamran University of Ahvaz, 6135743169 Ahvaz, Iran

[b] Department of Chemistry, College of Science, Shiraz University, 7194684795 Shiraz, Iran. E-mail: v.nobakht@saadi.shirazu.ac.ir

†Electronic supplementary information (ESI) available. See DOI: https://doi.org/10.1039/d5dt01213a

Post-synthetic modification (PSM) has emerged as a powerful strategy to overcome the challenges associated with the synthesis of CPs by enabling the functionalization or tuning of CPs after their initial synthesis, without altering their original crystal topology. The first report of PSM in CPs involved the replacement of aqua ligands at coordinatively unsaturated sites (CUSs) in HKUST-1 with pyridine molecules.[36] Since then, numerous reports on the post-synthetic treatment of CPs have been published.[37–40] Generally, PSM approaches have expanded considerably and are classified into three main types: modifying organic linkers, exchanging or modifying metal nodes, and manipulating guest species *via* removal, substitution, adsorption, and oxidation/reduction processes.[35] This strategy allows the introduction of functional groups that might be incompatible with direct synthesis, simplifies multifunctionality, and prevents unpredictable reactions.[41] Additionally, PSM techniques have been utilized to produce single-layer 2D metal–organic nanosheets (MONs) by exfoliation or selective ligand removal, as well as to construct 3D supramolecular architectures through covalent cross-linking.[11,16,42–44]

In this study, we report tandem post-synthetic modifications on a 2D Zn-based coordination polymer (**Zn-CP**), resulting in the formation of exfoliated nanosheets, cross-linked multilayers, and 3D supramolecular architectures through functionalization with acid–base agents (Scheme 1). The **Zn-CP** was synthesized using our previously reported procedure, with significant improvements in the preparation method that led to a higher reaction yield.[45] The structural transformations induced by these post-synthetic modifications were thoroughly characterized and compared to the parent **Zn-CP**. Furthermore, to assess the influence of these structural modifications on functional performance, the adsorption behavior of the materials toward both anionic and cationic dyes was systematically investigated.

Experimental

Materials and instrumentation

The solvents were purchased from commercial suppliers Merck and Carlo. The starting materials were purchased from Merck, including $Zn(NO_3)_2 \cdot 6H_2O$ (CAS No.: 10196-18-6), 5-aminoisophthalic acid (CAS No.: 99-31-0), ethylenediamine (CAS No.: 107-15-3), 1,3-diaminopropane (CAS No.: 109-76-2), and 1,3-propanesultone (CAS No.: 1120-71-4).

Infrared spectra (4000–400 cm^{-1}) were recorded as KBr discs using a PerkinElmer Spectrum Two FT-IR spectrometer. Elemental analyses for C, H, N, and S were performed on an Elementar Vario EL III CHNS analyzer. Thermogravimetric analysis (TGA) was conducted on a Linseis PT1600 simultaneous thermal analyzer at a heating rate of 10 °C min^{-1} in the temperature range of 25–1000 °C. Powder X-ray diffraction (PXRD) patterns were recorded on a Panalytical X'PertPro diffractometer (Cu Kα radiation, λ = 1.54184 Å) in the 2θ range of 5–50°. Zeta potentials were measured using a Malvern Zetasizer Nano ZS (Version 7.03) with samples dispersed in ethanol at a concentration of 100 ppm. FE-SEM images were acquired using a Mira 3-XMU scanning electron microscope operated at an acceleration voltage of 20 kV. TEM imaging was carried out using a LEO 906E microscope at 40–120 kV, with a magnification of up to 600 000× and a resolution of 0.34 nm. Ultraviolet–visible (UV–Vis) spectra were measured using a Jasco V-730 spectrophotometer in the wavelength range of 400–700 nm, with a resolution of 0.2 nm and a scan speed of
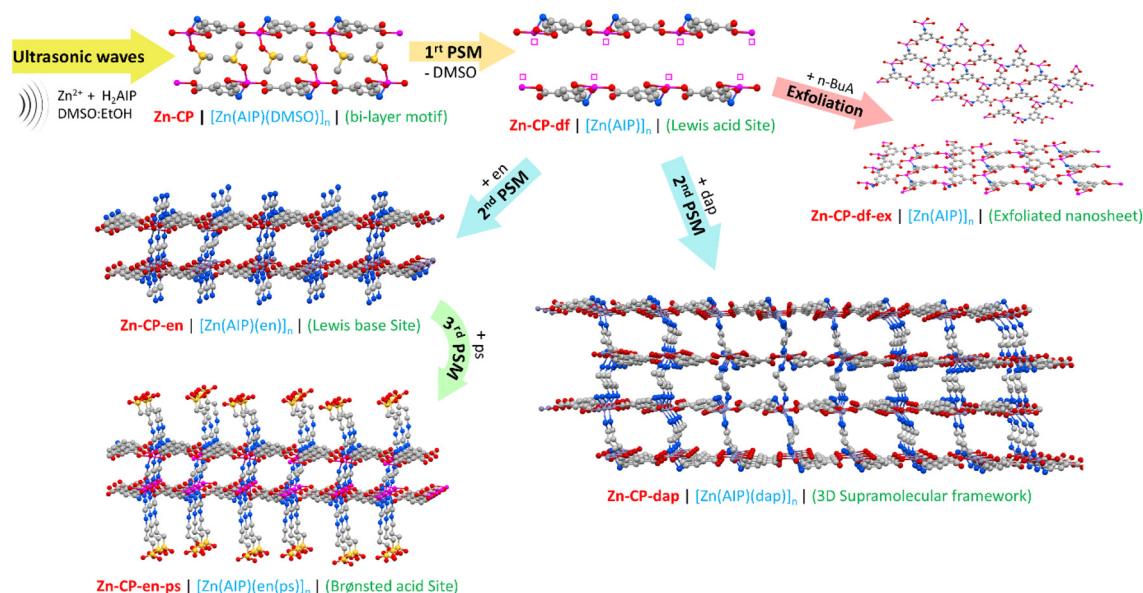
Scheme 1 Schematic illustration of the tandem PSM process on **Zn-CP** and its modified derivatives. (Gray: carbon, blue: nitrogen, red: oxygen, and yellow: sulfur. Hydrogen atoms are omitted for clarity.)

400 nm per minute. X-ray crystallographic data for **Zn-CP**, our previously reported structure[45] (CCDC: 2011679), were collected using Mo Kα radiation on a Bruker APEX II diffractometer. The structure was solved by direct methods and refined using full-matrix least-squares on F^2, with hydrogen atoms placed at geometrically calculated positions. The disordered DMSO ligand was refined with soft restraints, and crystallographic data are summarized in Table 1.

Synthesis of $[Zn(AIP)(DMSO)]_n$ (Zn-CP)

$[Zn(AIP)(DMSO)]_n$ (**Zn-CP**) was prepared according to our previous report with significant modifications that increased the product yield from 65% to 96% and reduced the size to the nano-scale. Zn $(NO_3)_2 \cdot 6H_2O$ (2.97 g, 10 mmol) was dissolved in a 25 mL mixture of DMSO and ethanol (2 : 1) in a 100 mL round-bottom flask (solution A). The H$_2$AIP ligand (1.81 g, 10 mmol) was dissolved in 25 mL of the same solvent (solution B), and triethylamine (TEA) (2.8 mL, 20 mmol) was dissolved separately in 25 mL of ethanol (solution C). Solution A was sonicated at 75 °C, and solutions B and C were simultaneously added dropwise to solution A over 150 minutes. The resulting white powder of **Zn-CP** was isolated by centrifugation, washed with ethanol (3 × 15 mL), and dried at 70 °C overnight (3.01 g, yield: 96% based on Zn). Anal. calcd (%) for $C_{10}H_{11}NO_5SZn$ (**Zn-CP**): C, 37.22; H, 3.43; N, 4.34; S, 9.93. Found (%): C, 37.18; H, 3.74; N, 4.56; S, 9.96.[45]

Synthesis of $[Zn(AIP)]_n$ (Zn-CP-df)

To eliminate DMSO molecules from the **Zn-CP** structure in the first step of PSM, 2.0 g (6.2 mmol) of **Zn-CP** was stirred in 50 mL of acetonitrile at room temperature for 12 h. This process was repeated four times to eliminate all coordinated solvent molecules from the network, with each cycle followed by filtration through centrifugation to isolate the precipitate. The resulting white powder was dried at 60 °C overnight. The product is referred to as **Zn-CP-df** (**Zn-CP-DMSO-free**). Found (%) for **Zn-CP-df**: C, 35.95; H, 2.71; N, 4.97; S, 0.94.

Synthesis of $[Zn(AIP)(en)]_n$ (Zn-CP-en)

The freshly synthesized **Zn-CP-df** (1.0 g, 4.0 mmol) was dispersed in 30 mL of toluene by sonication. The mixture was stirred gently at 100 °C while ethylenediamine (en) (0.3 mL, 4.5 mmol) was added dropwise, and then the reaction mixture

was refluxed for 24 h to complete the second step of the PSM process. The supernatant was separated by centrifugation, and the white product was washed with toluene (2 × 10 mL) and ethanol (1 × 10 mL) and dried at 75 °C for 6 hours to obtain **Zn-CP-en** (**Zn-CP-ethylenediamine**). Found (%) for **Zn-CP-en**: C, 35.14; H, 4.59; N, 13.81; S, 0.60.

Synthesis of $[Zn(AIP)(dap)]_n$ (Zn-CP-dap)

In parallel with the second step of the PSM, the synthesis of **Zn-CP-dap** (**Zn-CP-1,3-diaminopropane**) was carried out following the same procedure using 1,3-diaminopropane (dap) (0.4 mL, 4.8 mmol). Found (%) for **Zn-CP-dap**: C, 41.01; H, 4.79; N, 12.62; S, 0.52.

Synthesis of $[Zn(AIP)(en)(ps)]_n$ (Zn-CP-en-ps)

In the third step of the PSM, 0.3 mL (3.4 mmol) of 1,3-propanesultone (ps) was slowly added to 1.0 g (3.0 mmol) of well-suspended **Zn-CP-en** in 50 mL of toluene at 70 °C. The mixture was then heated under reflux for 24 h. The resulting precipitate was separated by centrifugation, washed with dichloromethane (2 × 10 mL) and ethanol (1 × 10 mL), and dried overnight at 60 °C. The yellowish-white powder of **Zn-CP-en-ps** was stored in a desiccator. Found (%) for **Zn-CP-en-ps** (%): C, 35.01; H, 4.12; N, 9.22; S, 5.58.

Synthesis of exfoliated $[Zn(AIP)]_n$ (Zn-CP-df-ex)

n-Butylamine (n-BuA) was used to exfoliate the bulk **Zn-CP-df**. Prior to adding n-BuA, **Zn-CP-df** was sonicated in 30 mL of toluene at 70 °C for 45 min. Then, 0.15 mL (0.2 mmol) of n-BuA was added dropwise to the sonicated suspension. The mixture was stirred under reflux conditions for 18 h. The resulting white precipitate of **Zn-CP-df-ex** (**exfoliated Zn-CP-df**) was separated by centrifugation, washed with n-hexane (2 × 10 mL), and dried overnight at 70 °C. Found (%) for **Zn-CP-df-ex**: C, 33.29; H, 2.21; N, 4.77; S, 0.43.

pH metric titration

The amount of terminal amine groups on the surfaces of **Zn-CP-en** and **Zn-CP-dap** was measured using acid–base titrations based on the works reported in the literature.[46,47] Hence, 0.025 g each of **Zn-CP-en** and **Zn-CP-dap** were suspended separately in 5 mL of DI water and stirred for 30 minutes at room temperature. The solid phase was separated by centrifugation, and the filtrate was titrated with 0.01 mol L^{-1} HCl in the presence of phenolphthalein as an indicator. The amount of terminal amine groups was determined from the titration data.

Dye adsorption experiment

The dye adsorption performance of **Zn-CP** and its modified derivatives was evaluated using Aniline Blue, Methyl Orange, and Congo Red as anionic dyes, and Brilliant Green, Malachite Green, and Methyl Green as cationic dyes *via* a batch adsorption method. For each test, 3 mL of dye solution was added to separate vials containing 10 mg of adsorbent material. The initial concentrations of Aniline Blue, Methyl Orange, Malachite Green, and Methyl Green were 100 ppm, while those

Table 1 Selected crystallographic data for **Zn-CP**[47]

	Zn-CP
Formula	$C_{10}H_{11}NO_5SZn$
Formula mass	322.65
Crystal system	Monoclinic
Space group	$P2_1/c$
a (Å)	9.8364(16)
b (Å)	7.6758(13)
c (Å)	16.125(3)
β (°)	95.100(2)
V (Å^3)	1212.7(4)
Z	4
D_{calcd} (g cm^{-3})	1.767

of Congo Red and Brilliant Green were 50 ppm. The mixtures were stirred continuously until adsorption equilibrium was reached, and then the adsorbent was separated by centrifugation. The remaining dye concentrations in the supernatant were determined using UV-Vis spectrophotometry, with quantification achieved through pre-established calibration curves. The removal efficiency (%) was calculated using eqn (1):

$$\% \ removal = \frac{C_0 - C_e}{C_e} \times 100 \tag{1}$$

where C_0 and C_e correspond to the initial and equilibrium dye concentrations (mg L^{-1}), respectively. All experiments were conducted in duplicate at 25 °C to ensure reproducibility.

Results and discussion

The crystal structure of **Zn-CP** was thoroughly discussed in our published work.[45] Briefly, as shown in Fig. 1a, in the 2D structure of **Zn-CP**, each zinc ion is coordinated by five atoms; one nitrogen and three oxygen atoms from three distinct AIP^{2-} linkers, with the fifth coordination site occupied by an oxygen atom from a DMSO molecule. Notably, the DMSO molecules coordinate to Zn only on one side of the sheets. Two adjacent sheets are oriented in opposite directions and displaced relative to each other, allowing the DMSO molecules to interdigitate into the interlayer region. In the 2D layers, each metal center connects via μ_3-AIP linkers and the oxygen atom of DMSO, adopting a ZnO$_4$N coordination environment. The geometry of the central Zn^{2+} ions lies between trigonal-bipyramidal and square-pyramidal, according to the calculated τ_5 factor ($\tau_5 = 0.6$). These Zn^{2+} ions connected by μ_3-AIP^{2-} linkers generate 2D layers extending along the *bc*-plane with a **6³-hcb** topology (Fig. S1†). The adjacent layers exhibit an ABAB slipped packing along the *a*-axis, stabilized by the interlayer interdigitation of DMSO molecules. These supramolecular features, including layer orientation, slipped stacking, and DMSO interdigitation, play a crucial role in enabling the post-synthetic modifications reported here by maintaining structural integrity while allowing for controlled exfoliation and cross-linking.
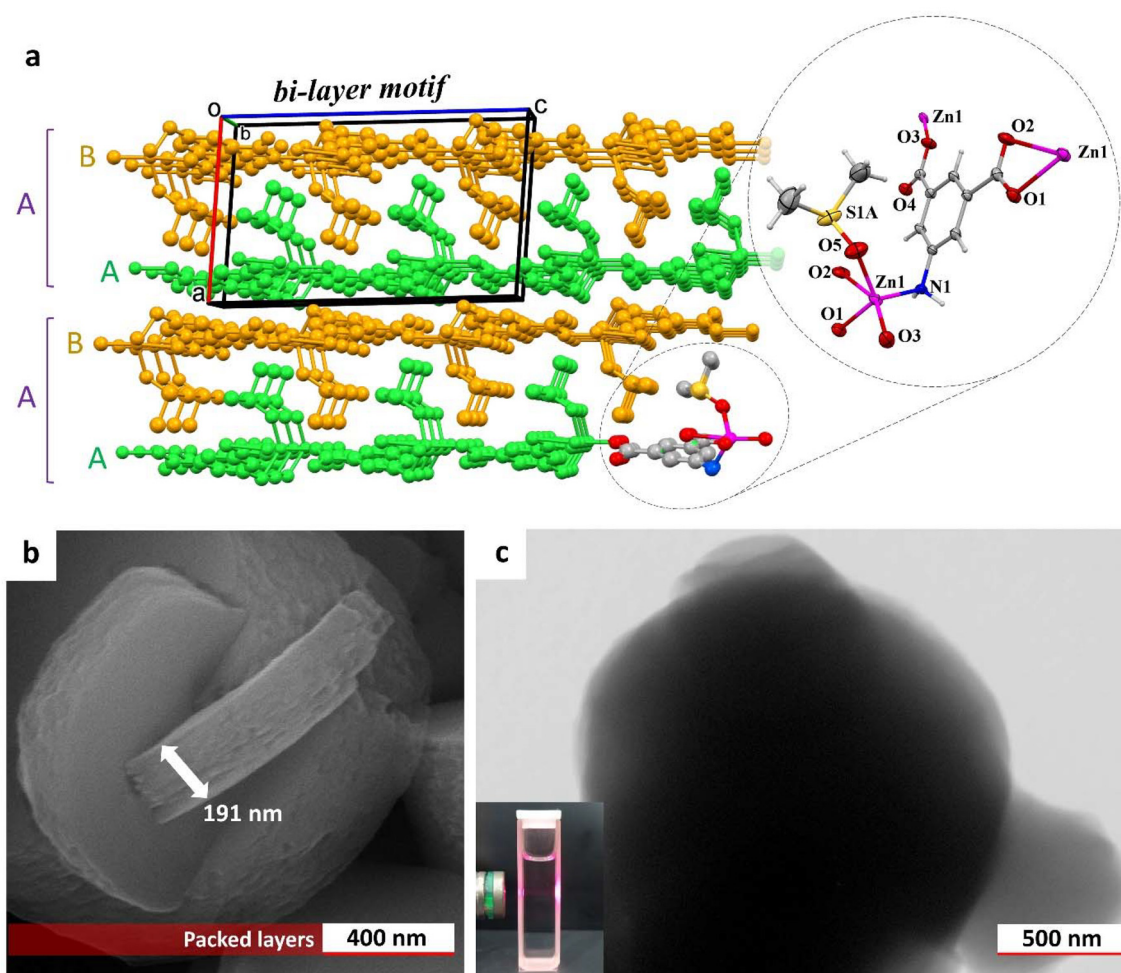

Fig. 1 The structure of **Zn-CP**. (a) View of the asymmetric unit, two adjacent layers, and the orientation of DMSO molecules in the crystal packing of **Zn-CP** (hydrogen atoms omitted for clarity). (b and c) FE-SEM and TEM images of **Zn-CP** (inset in c: the Tyndall effect of an ethanolic colloidal suspension of **Zn-CP** after centrifuging at 8000 rpm).

Zinc is a highly versatile transition metal that can form complexes with coordination numbers of four, five, and six, each with different geometries. Due to its zero-ligand field stabilization energy and d^{10} configuration, the final geometry of its complexes depends only on the steric hindrance of the organic ligands.[48] In light of this information, and with the aim of forming Lewis acid sites, DMSO molecules were removed from the zinc central atoms of the **Zn-CP** structure in the initial step of PSM. This reduced the coordination number of the metal centers from five to four, resulting in the formation of **Zn-CP-df** with a coordinatively unsaturated site (CUS).

In order to exfoliate the stacked layers of **Zn-CP-df** into separate thin layers, the compound was exposed to *n*-butylamine (*n*-BuA) as an amine functional group with a long flexible alkane chain. This process resulted in the formation of exfoliated **Zn-CP-df-ex** nanosheets without the formation of any chemical bonds between *n*-BuA and the CUS of **Zn-CP-df**, as illustrated in Fig. 3a. Exfoliation and the formation of the ultrathin nanosheet layers were also confirmed by observing

the Tyndall effect when a laser beam passes through an ethanolic solution of the compounds in a quartz cell (as seen in image c of Fig. 1–6). It can be concluded that **Zn-CP-df-ex** exhibits a stronger Tyndall effect compared to **Zn-CP-df**, while as expected **Zn-CP** has no Tyndall effect. There are several reports on the Tyndall effect of exfoliated MOFs, confirming the successful formation of ultrathin 2D layers.[49–51]

To create Lewis base sites on the surface of the layers, in the second step of the PSM, ethylenediamine (en) and 1,3-diaminopropane (dap) were separately added as amine functional groups to **Zn-CP-df**. This resulted in the formation of **Zn-CP-en** and **Zn-CP-dap** by coordinating the nitrogen atoms of the amine groups to the CUS of **Zn-CP-df**.

On the other hand, the structure of **Zn-CP-dap** consists of a 3D supramolecular framework formed by cross-linking **Zn-CP-df** layers *via* dap linkers, as can be seen in the microscopic images (Fig. 5). Moreover, no significant Tyndall effect was observed for this structure, confirming the connection of adjacent 2D layers into a 3D framework.
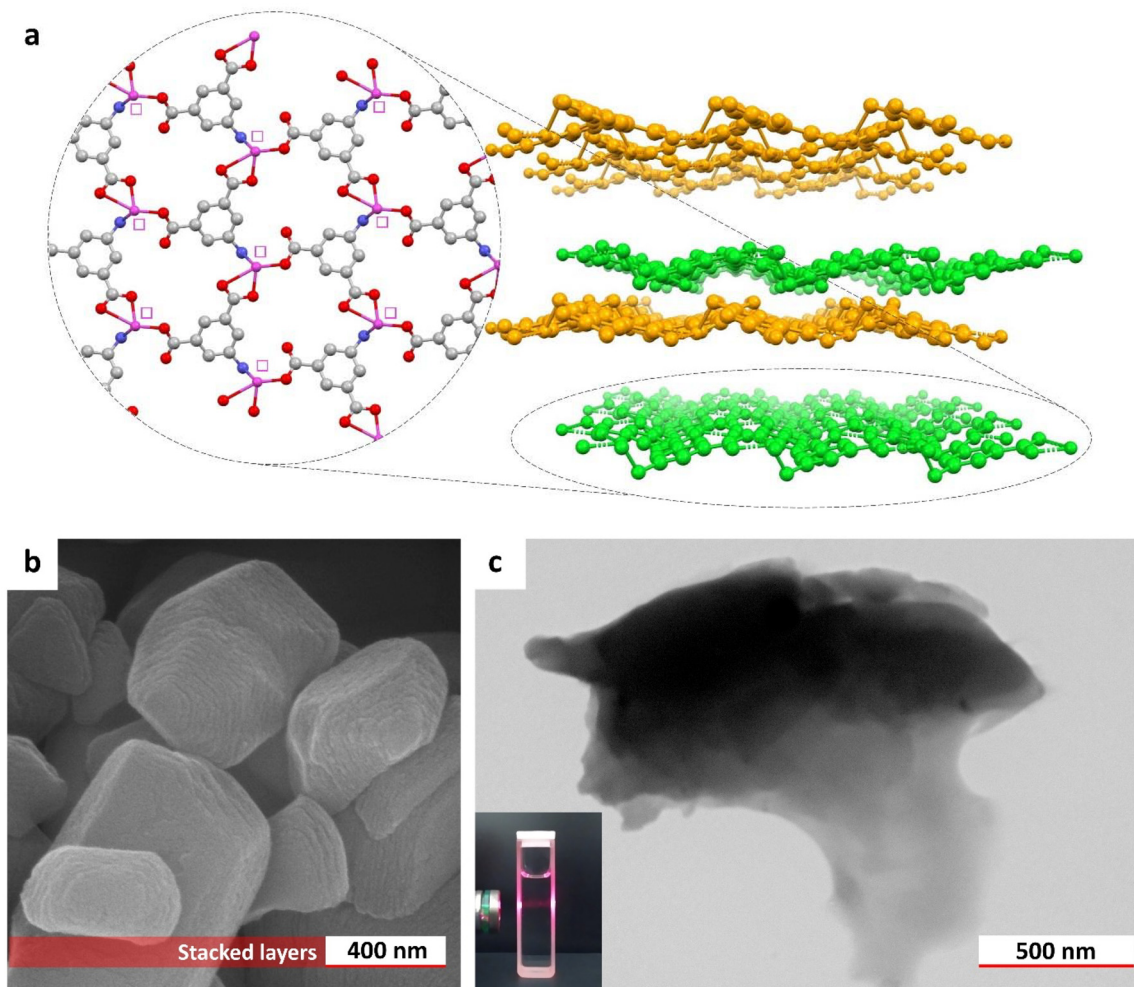

Fig. 2 (a) Suggested structure of **Zn-CP-df** with stacked layers as the first product of PSM (each square represents a CUS or Lewis acid site). (b and c) FE-SEM and TEM images of **Zn-CP-df** (inset in c: the Tyndall effect of an ethanolic colloidal suspension of **Zn-CP-df** after centrifuging at 8000 rpm).
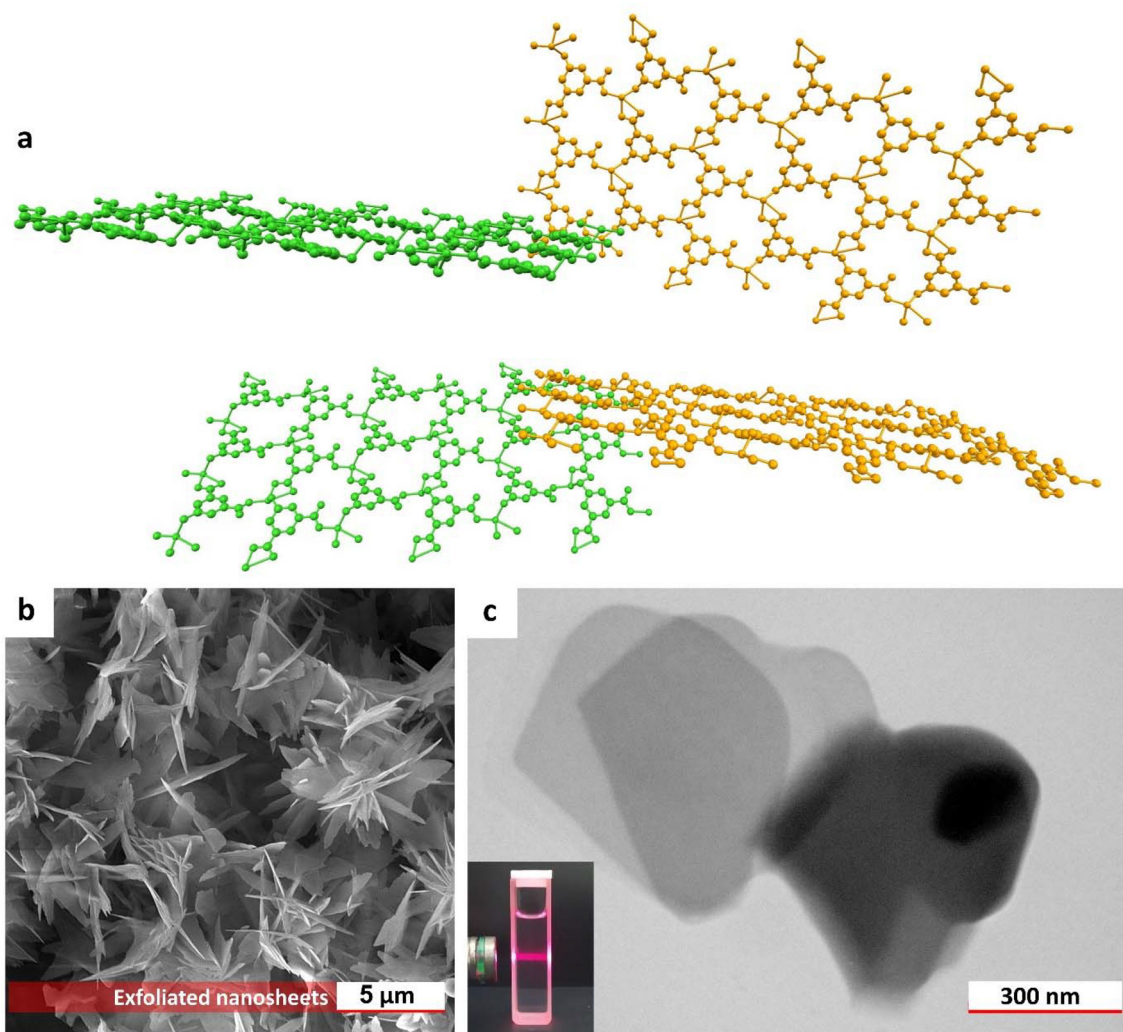
Fig. 3 (a) Suggested structure of the exfoliated **Zn-CP-df-ex** nanosheets. (b and c) FE-SEM and TEM images of **Zn-CP-df-ex** (inset in c: the Tyndall effect of an ethanolic colloidal suspension of **Zn-CP-df-ex**).

Next, in order to create Brønsted acid sites on the surface of the layers, in the third step of tandem PSM, **Zn-CP-en** was reacted with 1,3-propanesultone (ps) to generate sulfonic acid functional groups on the surface of **Zn-CP-en**. Terminal methylene units of the ps molecules, after ring-opening, have great tendency to react with the terminal amine groups of **Zn-CP-en**, resulting in the formation of **Zn-CP-en-ps** as depicted in Fig. 6.

As the cross-linking in the second and third steps of PSM promotes the agglomeration of the sheets, the Tyndall effect is weakened due to the settling of the particles in ethanol (Fig. S2†). As a result, the process of functionalization is visible at each stage of the PSM accompanied by changes in the Tyndall effect.

The proposed structures of the **Zn-CP** derivatives are supported by FE-SEM and TEM analyses, Tyndall effect observations, FT-IR spectroscopy, PXRD, zeta-potential measurements, EDX mapping, and CHNS elemental analysis.

Morphological studies

FE-SEM and TEM images (Fig. 1b and c) of **Zn-CP** confirm the presence of tightly packed, smooth 2D thin layers with lateral dimensions in the micron range and an average thickness of approximately 200 nm, indicating the formation of a well-defined layered structure. After the removal of solvent molecules, **Zn-CP-df** retains its layered morphology, with similar thickness and lateral dimensions, as evidenced by FE-SEM and TEM images (Fig. 2). Upon exfoliation, **Zn-CP-df-ex** exhibits effective delamination of the layers, resulting in nanosheets with a reduced thickness of ~20 nm and an average lateral size of 3.2 μm (Fig. 3b and S3†). The TEM image (Fig. 3c) reveals almost transparent exfoliated layers. The delamination of bulk-stacked layers of **Zn-CP-df** into nanosheets of **Zn-CP-df-ex** is clearly shown in Fig. S4.† For **Zn-CP-en**, microscopic images (Fig. 4 and S5†) show that the layers adopt a disordered arrangement, forming a multilayered structure with an average
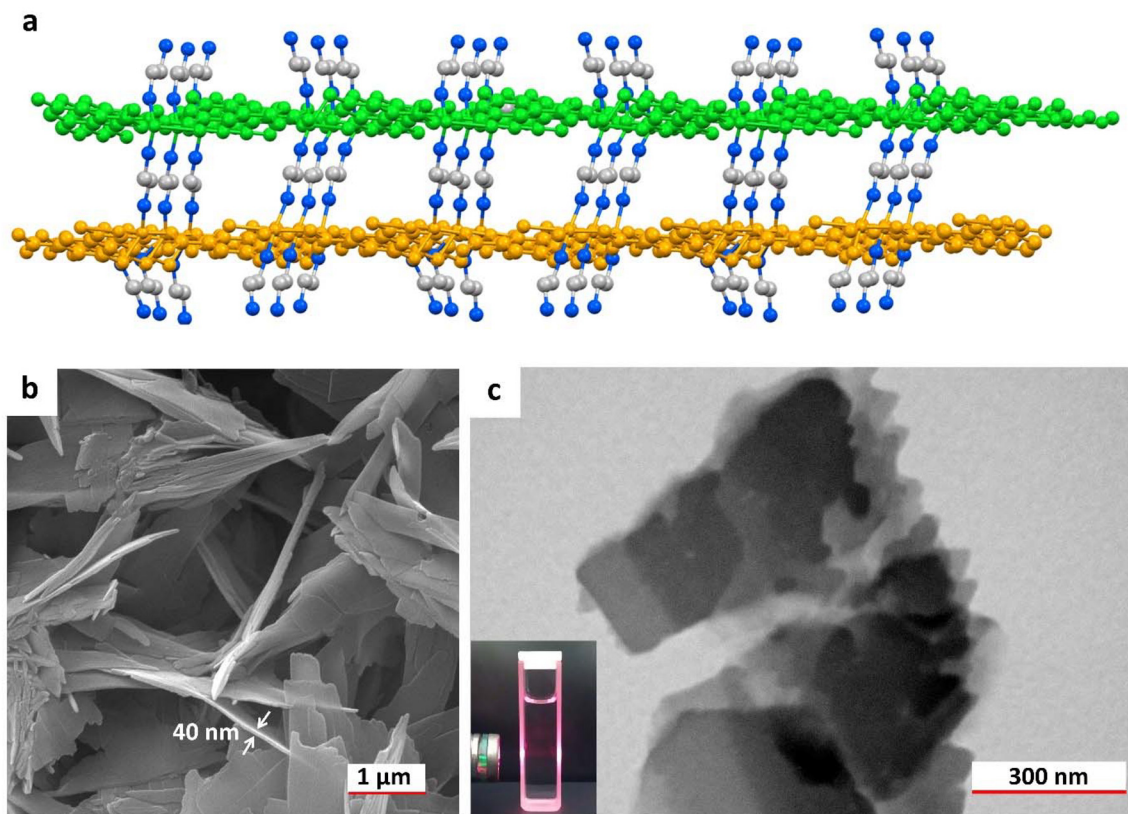
Fig. 4 (a) Suggested multilayer structure of **Zn-CP-en** as the second PSM product. (b and c) FE-SEM and TEM images of **Zn-CP-en** (inset in c: the Tyndall effect of an ethanolic colloidal suspension of **Zn-CP-en**).

thickness of ∼40 nm. This morphology likely results from cross-linking of **Zn-CP-df** layers by ethylenediamine linkers. Following treatment with 1,3-diaminopropane (DAP), the initially layered structure of **Zn-CP-df** transforms into a new interconnected 3D supramolecular framework (**Zn-CP-dap**) with semi-spherical morphologies, as observed in the FE-SEM and TEM images (Fig. 5b, c, and S6†). For **Zn-CP-en-ps**, the microscopic images (Fig. 6b, c, and S7†) reveal fragmentation and aggregation of the layers compared to **Zn-CP-en**. This aggregation is likely due to the introduction of –SO₃H groups, which increases hydrogen-bonding interactions between the layers. Collectively, these morphological studies confirm the structural evolution from layered nanosheets to cross-linked multilayers and eventually to interconnected 3D frameworks through post-synthetic modifications, supporting the functionalization pathways proposed in this study.

FT-IR spectroscopy

The structures of the PSM products were also investigated by FT-IR spectroscopy. In the FT-IR spectrum of **Zn-CP** (Fig. 7, blue), two absorption peaks with medium intensity at 3139 and 3253 cm^{-1} are assigned to the symmetric and asymmetric stretching vibrations of the N–H bonds of the AIP^{2-} ligand, respectively. This shows a red shift of about 23 cm^{-1} compared to free H₂AIP. The peaks with weak intensity around 3000 cm^{-1} are related to the aromatic C–H bonds of the AIP^{2-} ligand. The peak at 1029 cm^{-1} is assigned to the S–O stretching vibration of the DMSO molecule.[52] Two sets of strong bands observed in the ranges of 1300–1400 and 1550–1650 cm^{-1} in the FT-IR spectra of the **Zn-CP** derivatives are attributed to the symmetric and asymmetric stretching vibrations of carboxylate C=O groups, respectively.[53] The areas highlighted in blue in Fig. 7 show the unchanged parts of the **Zn-CP** network during the tandem PSM process. As can be seen in Fig. 7, there is no obvious difference between the infrared spectra of **Zn-CP-df** and **Zn-CP-df-ex** compared to the spectrum of the pristine **Zn-CP** structure, and it is difficult to trace the removal of DMSO molecules in the FT-IR spectra of the DMSO-free products **Zn-CP-df** and **Zn-CP-df-ex**; however, a significant decrease in sulfur content from 9.96 to 0.95% in elemental analyses confirms the effective removal of DMSO molecules. The weakening of the N–H vibrational bands in the infrared spectrum of **Zn-CP-df-ex** compared to **Zn-CP** can be attributed to the loss of intermolecular hydrogen bonds, due to the exfoliation of the adjacent layers.

With the addition of ethylenediamine in the second PSM step and the formation of **Zn-CP-en** (Fig. 7, brown), three new peaks with medium intensity appear in the range of 3300 to 3400 cm^{-1} (yellow zone), corresponding to two different types of free and coordinated amine groups.[54] The N–H stretching
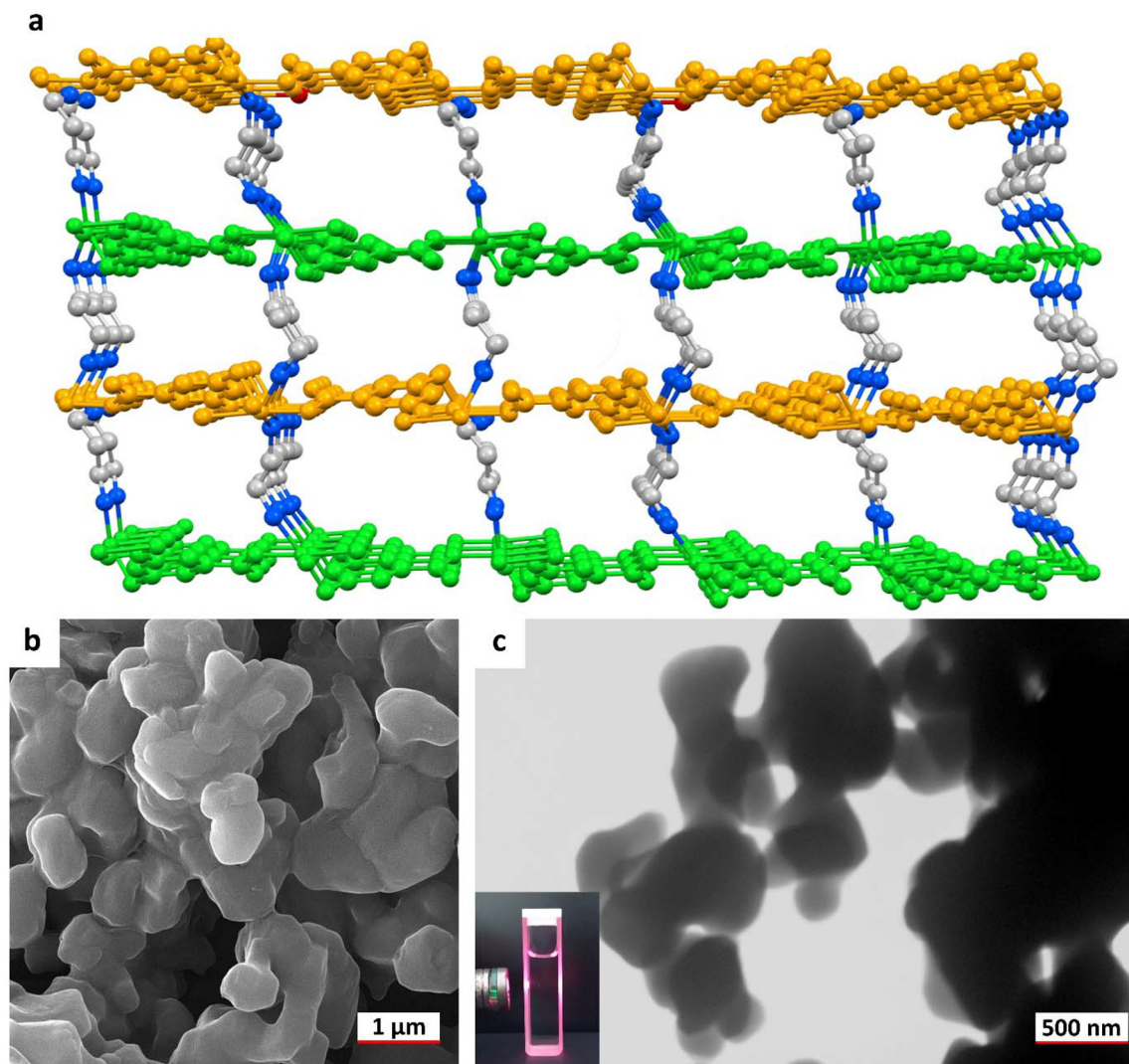
Fig. 5 (a) Suggested structure of the 3D supramolecular framework of **Zn-CP-dap** as the second PSM product. (b and c) FE-SEM and TEM images of **Zn-CP-dap** (inset in c: the Tyndall effect of an ethanolic colloidal suspension of **Zn-CP-dap**).

bands of en in the FT-IR spectrum of **Zn-CP-en** appear at higher frequencies than the N–H vibrations of the AIP^{2-} ligand.[55] Similarly, in the case of **Zn-CP-dap** (Fig. 7, purple), two distinct strong peaks are observed in the yellow zone, attributed to the N–H vibrations of the dap groups. In the third PSM step, ps molecules are connected to the surface terminal amine groups of **Zn-CP-en**, generating **Zn-CP-en-ps**. The successful formation of **Zn-CP-en-ps** is confirmed by the presence of some new bands corresponding to the asymmetric stretching vibration of the O=SO=O functional group at 1040[56] and a band at 3505 cm^{-1} corresponding to SO–H groups (red zones in Fig. 7).

Powder X-ray diffraction

To investigate the crystallinity of the **Zn-CP** derivatives and the structural changes during the PSM process, PXRD analysis was also carried out. As shown in Fig. 8, the PXRD patterns of the

as-synthesized **Zn-CP** and **Zn-CP-df** are consistent with the structure obtained from single-crystal X-ray diffraction. As expected, the removal of DMSO molecules did not have a significant effect on the structure of **Zn-CP**, and the bulk **Zn-CP-df** retained its layered structure along the [100] direction.

To investigate the possibility of exfoliating bulk **Zn-CP-df**, *n*-butylamine (*n*-BuA), a long flexible alkane-chain amine, was used as an exfoliating agent to separate the stacked layers. The results of the PXRD analysis along with FE-SEM and TEM images clearly show that the stacked layers in **Zn-CP-df** have been exfoliated into **Zn-CP-df-ex**, and some changes in its PXRD pattern can be attributed to the separation of stacked layers and conversion into nanosheets. Similarly, the PXRD patterns of **Zn-CP-en** and **Zn-CP-en-ps** further align with the PXRD patterns of **Zn-CP-df-ex**, suggesting a multilayered or sheet-like structure for these derivatives. The absence of changes in most of the diffraction peaks, such as (11−1), (112),
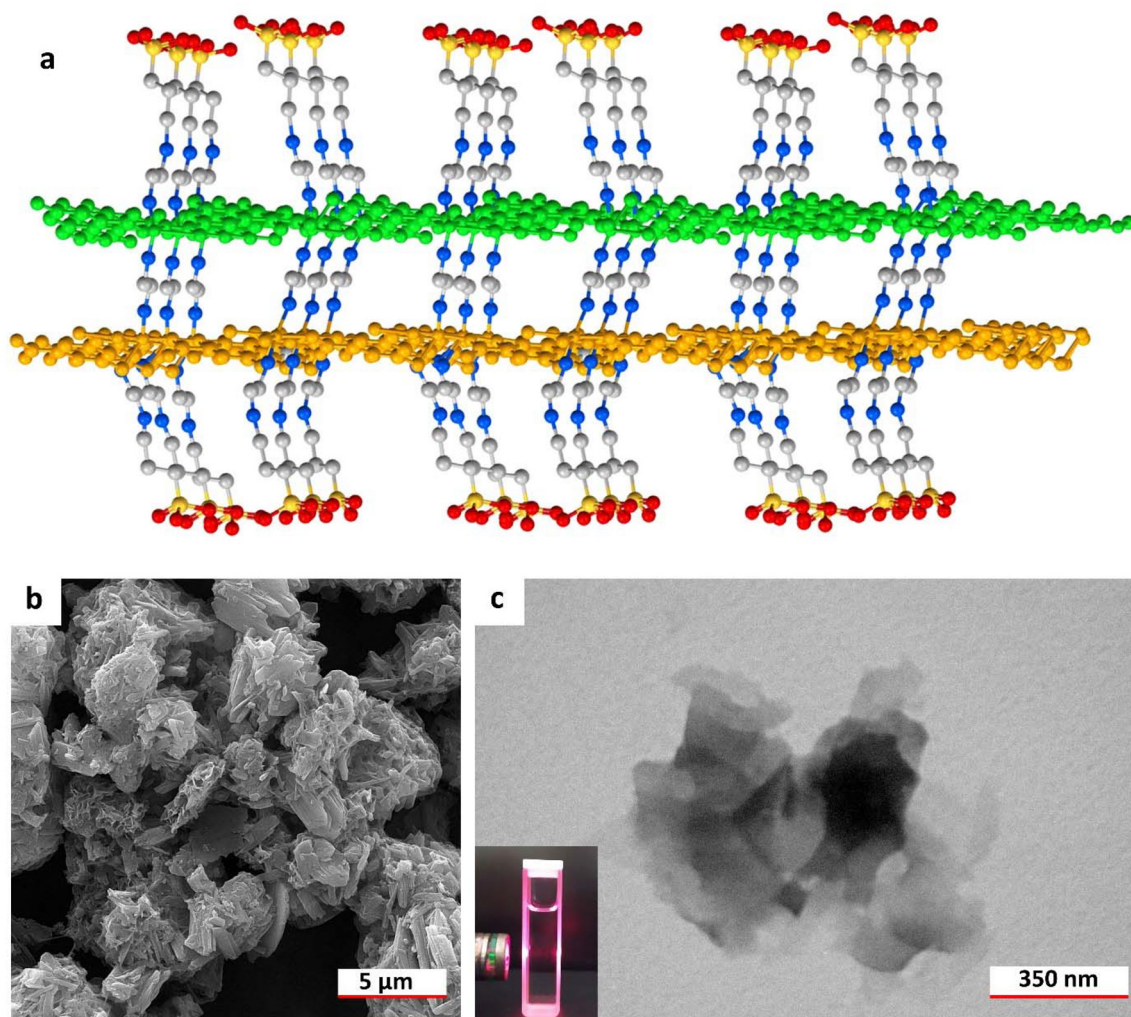
Fig. 6 (a) Suggested multilayer structure of **Zn-CP-en-ps** as the third PSM product. (b and c) FE-SEM and TEM images of **Zn-CP-en-ps** (inset in c: the Tyndall effect of an ethanolic colloidal suspension of **Zn-CP-en-ps**).
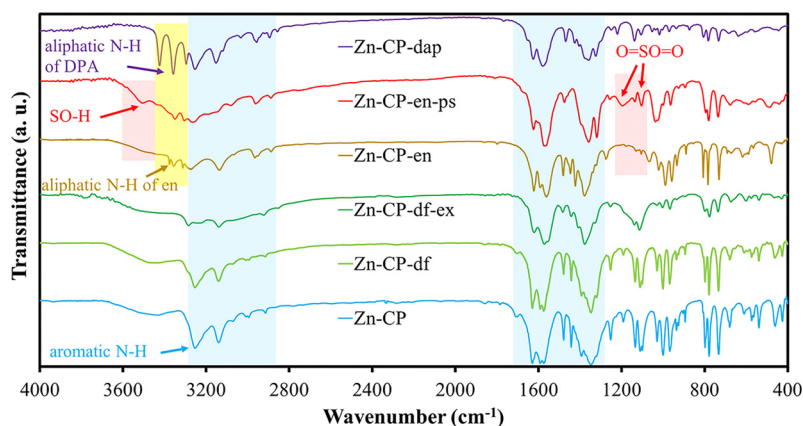

Fig. 7 The FT-IR spectra of the as-synthesized **Zn-CP** and its derivatives after each step of PSM.

and (300) planes, shows that the structure of the 2D network remains intact. However, a shift in the (100) diffraction peaks to lower 2-theta values is consistent with the increase in the size of the inter-layer functional groups between bi-layer motifs, as already observed in isostructural zinc-AIP polymers, $[\text{Zn}(\text{AIP})(\text{solvent})]_n$, where the coordinated molecules are N,N-
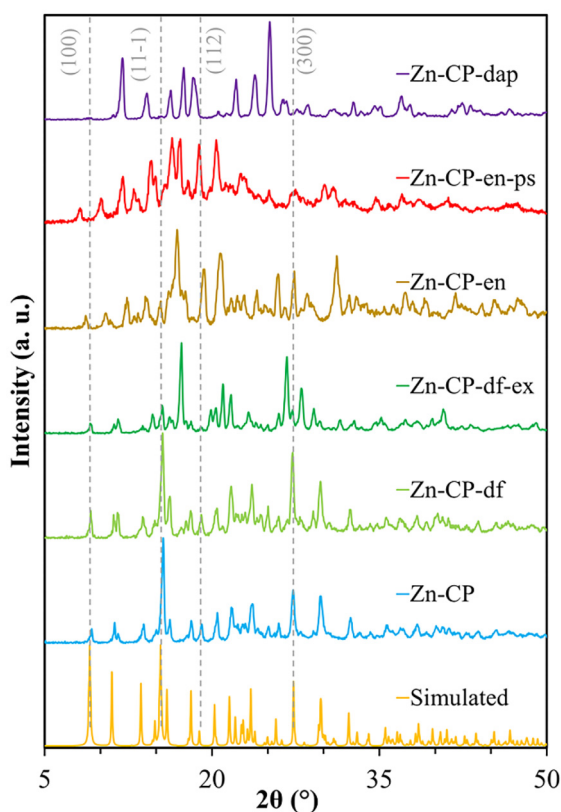
Fig. 8 Simulated and experimental PXRD patterns of **Zn-CP** and its PSM derivatives. The gray vertically dotted lines indicate the positions of indexed diffractions.

PXRD of **Zn-CP-df**, due to the formation of a 3D supramolecular framework facilitated by the dap molecules. The dap molecule seems to act as a cross-linking agent between the stacked layers of **Zn-CP-df**, resulting in a new diffraction pattern by changing the arrangement of the layers in the unit cell, without destroying the 2D network. Elemental and thermogravimetric analyses, and photophysical properties were used to confirm these findings.

Elemental analysis

The composition of **Zn-CP** and its modified compounds was evaluated using energy-dispersive X-ray (EDX) spectroscopy and elemental mapping (Fig. 10). The results show an appropriate distribution of the constituent elements. Complementary investigations on the composition of the products were also carried out using CHNS elemental analysis.

Elemental analysis is a valuable technique to monitor the PSM process. Table 2 shows a comparison of elemental analysis (CHNS) results with simple stoichiometric calculations (SC) for the parent **Zn-CP** and its PSM derivatives. In addition, pH-metric titration (pH-m) was also performed to determine the amount of terminal $-NH_2$ groups in **Zn-CP-en** and **Zn-CP-dap** through acid–base titration.[46,47]

Initially, based on a comparison of the results of CHNS analysis with SC data, it was anticipated that in the structure of **Zn-CP-en**, each en molecule would be connected to a zinc CUS through only one amine group, leading to 5-coordinate centers similar to the **Zn-CP** structure, but pH-m results revealed additional insights as depicted in Fig. 2–6.

According to the results of the CHNS analysis given in Table 1, the nitrogen content in the structure of **Zn-CP-df** is 4.97%, all of which is related to the nitrogen atoms of the AIP^{2-} ligand. In comparison, the nitrogen content in **Zn-CP-en** increased to 13.81%. The difference between these two amounts (8.84%) is attributed to the nitrogen of the en molecules (either coordinated or uncoordinated amines) in the structure of **Zn-CP-en**. The observation suggests that each type of nitrogen in the en

dimethylacetamide (DMA) and *N,N*-diethyl formamide (DEF) (Fig. 9).[57–59] The appearance of the new diffraction patterns next to the original diffraction patterns can be attributed to the changes in the arrangement of bi-layer motifs and modifications in the stacked layers through the second and third steps of the PSM. With respect to the **Zn-CP-dap** structure, the diffraction pattern is significantly altered compared to the
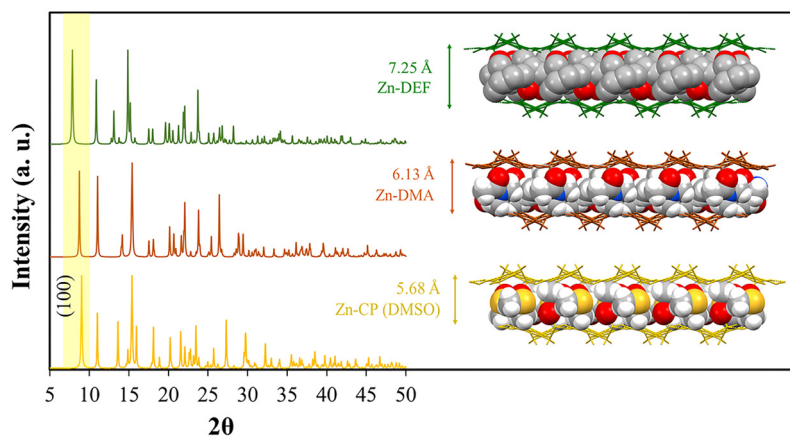

Fig. 9 Simulated PXRD patterns and interlayer distances in three related structures [Zn(AIP)(solvent)]$_n$, where the solvent is *N,N*-diethyl formamide (DEF), *N,N*-dimethylacetamide (DMA), and dimethyl sulfoxide (DMSO).
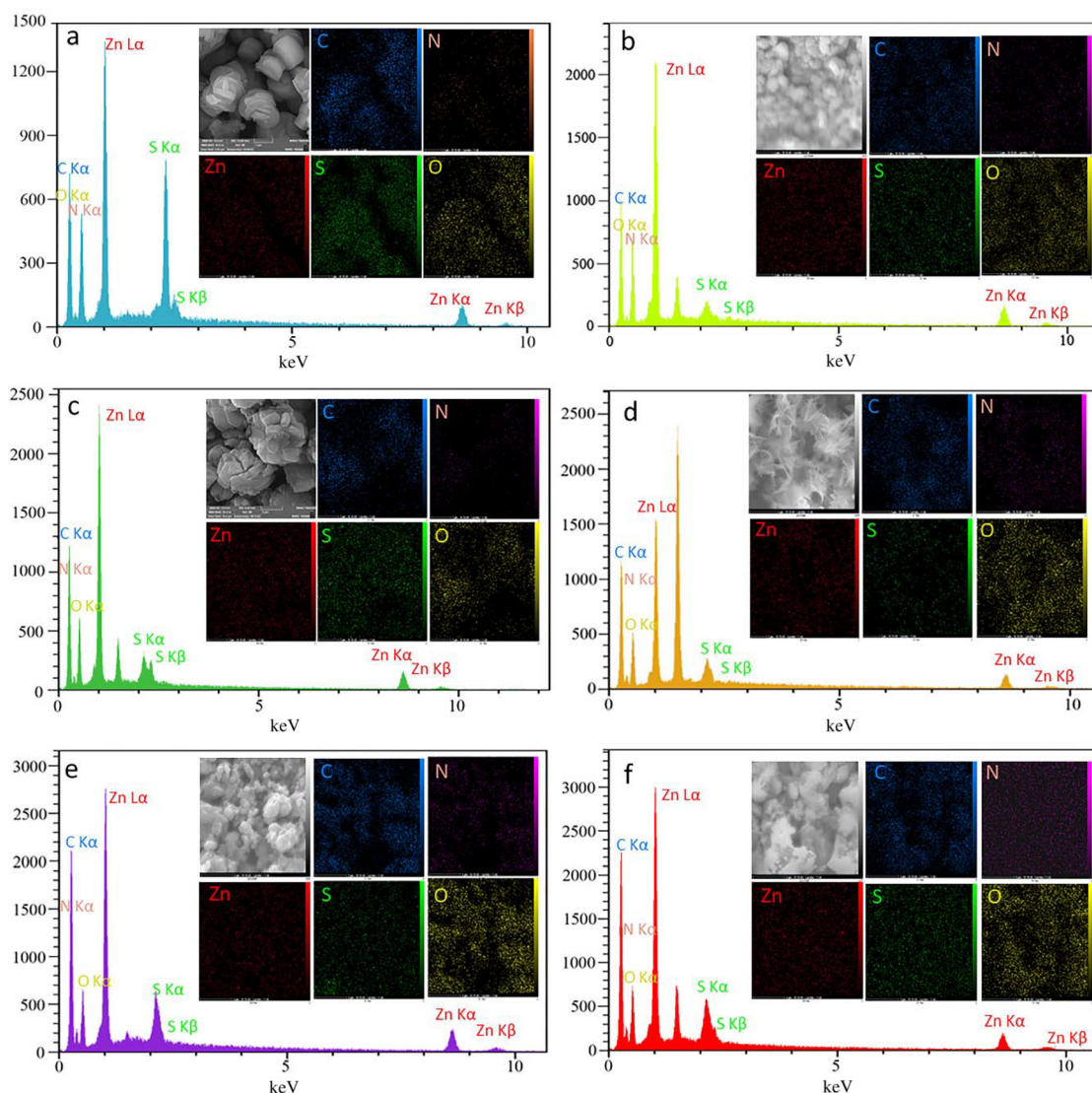
Fig. 10 EDX spectra with corresponding elemental mapping patterns of (a) **Zn-CP**, (b) **Zn-CP-df**, (c) **Zn-CP-df-ex**, (d) **Zn-CP-en**, (e) **Zn-CP-dap**, and (f) **Zn-CP-en-ps**.

Table 2 Comparison of elemental percentages in the structures of PSM products determined by SC[a], CHNS[b], and pH-m[c]

Element	Zn-CP		Zn-CP-df		Zn-CP-df-ex		Zn-CP-en			Zn-CP-dap			Zn-CP-en-ps	
	SC	CHNS	SC	CHNS	SC	CHNS	SC	CHNS	pH-m	SC	CHNS	pH-m	SC	CHNS
Carbon	37.22	37.18	39.90	35.95	39.90	33.29	39.43	35.14	—	41.47	41.01	—	36.59	35.01
Nitrogen	4.34	4.56	5.73	4.97	5.73	4.77	13.80	13.81	1.55	13.19	12.62	0.27	9.85	9.22
Sulfur	9.93	9.96	0	0.94	0	0.43	0	0.60	—	0	0.52	—	7.51	5.58
Hydrogen	3.43	3.74	2.06	2.71	2.06	2.21	4.30	4.59	—	4.74	4.79	—	4.49	4.12

[a] SC: stoichiometric calculations. [b] CHNS: elemental analysis data. [c] pH-m: pH-metric titration for determining terminal amines.

molecule (coordinated or terminal amine) contributes approximately 4.42%. However, the pH metric tests show an interesting result that out of the 8.84% of nitrogen content, only 1.55% of it is related to the terminal amine group and the rest is related to the coordinated amine groups. This significant amount of co-

ordinated amine groups is the reason for the recommended structure of **Zn-CP-en**, where en molecules act as cross-linking agents between two zinc centers of adjacent layers. Therefore, a multilayer structure, as depicted in Fig. 4a, is proposed for **Zn-CP-en**, which is consistent with the results of previous analyses.

Similarly, in the case of **Zn-CP-dap**, pH-m experiments indicate that the amount of terminal amine groups in its structure is negligible, at only 0.27%. This suggests that almost all dap molecules act as flexible bidentate cross-linking agents or pillared ligands, connecting adjacent layers to create a 3D framework, with only a limited number of terminal dap molecules (Fig. 5a).

In the third step of post-synthetic modification (PSM), the ps molecules bind to the terminal amine groups on the surface of **Zn-CP-en**. Elemental analysis revealed that the sulfur content in the final product **Zn-CP-en-ps** is 4.98%. To explain this, the original **Zn-CP-en** (before adding ps) contains 0.60% sulfur. After adding ps, the total sulfur rises to 5.58%, meaning 4.98% comes directly from the bonded ps molecules. This 4.98% sulfur content corresponds to 66% of the amine groups being modified (sulfonated), as the calculated maximum sulfur content for full modification would be 7.51%. This clarifies that most of the amine groups (but not all) successfully reacted with ps during the sulfonation process. On the other hand, ps molecules are not bonded to **Zn-CP-dap**, as almost all amine groups in this structure are coordinated to the zinc centers. In contrast to **Zn-CP-en-ps**, the FT-IR spectrum of the product of **Zn-CP-dap** treated with ps shows no evidence of ps binding to the amine groups of **Zn-CP-dap** (Fig. S8†).

Zeta potential

The surface charges of **Zn-CP** and its derivatives were measured *via* zeta potential analysis in ethanol at room temperature (Fig. 11). Understanding the surface charge is crucial because it directly affects the stability of the particles in suspension and governs the electrostatic interactions between the adsorbent surface and charged dye molecules. These interactions play a key role in the adsorption efficiency and selectivity. Therefore, measuring the zeta potential provides valuable insight into how functional groups such as $-NH_2$ and $-SO_3H$ alter the surface properties and influence adsorption behavior. As shown in Fig. 11, the zeta potential of **Zn-CP-df** (+36.8 mV) is significantly higher than that of **Zn-CP** (+9.58 mV), which can be attributed to the removal of approximately 90% of the DMSO molecules from the parent framework, exposing more

open metal sites and resulting in a highly positive surface charge.[60,61] For **Zn-CP-en**, the pH-metric indicates that only about 1.55% of the introduced $-NH_2$ groups are present as free terminal amines. These limited terminal amines account for the slight decrease (approximately 1.3 units) in zeta potential compared to the parent compound. In the case of **Zn-CP-dap**, the diamine linker bridges the layers *via* cross-linking, and thus, the $-NH_2$ groups are not freely exposed at the surface, based on the pH-metric studies. As a result, the zeta potential remains nearly unchanged compared to that for **Zn-CP**. For **Zn-CP-en-ps**, the observed decrease in zeta potential by approximately 3 units is consistent with the presence of highly electronegative $-SO_3H$ groups.[62] It is important to note that these sulfonic acid groups are grafted onto only 1.55% of the terminal amine moieties in **Zn-CP-en**. Therefore, a significant drop in zeta potential was not expected. Nevertheless, the greater decrease observed, compared to **Zn-CP-en**, can be attributed to the stronger electron-withdrawing nature and greater surface polarity of the $-SO_3H$ groups relative to $-NH_2$. In summary, the zeta potential trends align well with the structural modifications, reflecting the interplay between open metal sites, amine coordination, and sulfonic acid incorporation.

TG analysis

Thermogravimetric analysis (TGA) was conducted on **Zn-CP** and its modified compounds to assess their thermal stability and quantify surface functional groups in the temperature range of 20–1000 °C. As depicted in Fig. 12, **Zn-CP** initially experiences a weight loss above 355 °C due to the removal of coordinated DMSO molecules (23.5%), while **Zn-CP-en** shows a weight loss of about 10% above 100 °C, attributed to moisture elimination. In the TGA profiles of all compounds, a significant weight loss is observed with a steadily decreasing curve starting at about 350 °C and continuing up to 660 °C, except for **Zn-CP-en-ps**, which exhibits a longer decreasing curve from 255 °C to 780 °C, corresponding to the decomposition of its organic components. These weight losses are approximately 57%, 67%, 71%, 74%, and 73% for **Zn-CP**, **Zn-CP-df**, **Zn-CP-en**, **Zn-CP-en-ps**, and **Zn-CP-dap**, respectively, with a residue attributed to the formation of zinc oxide obtained through the calci-
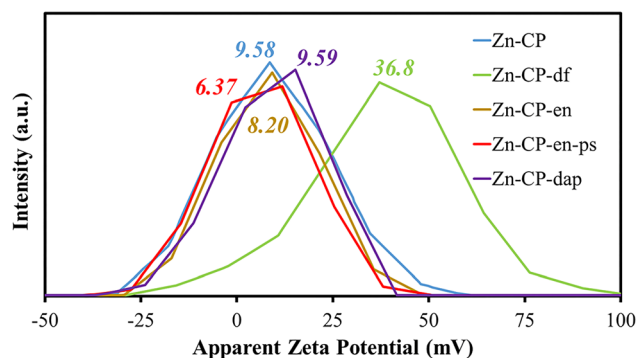

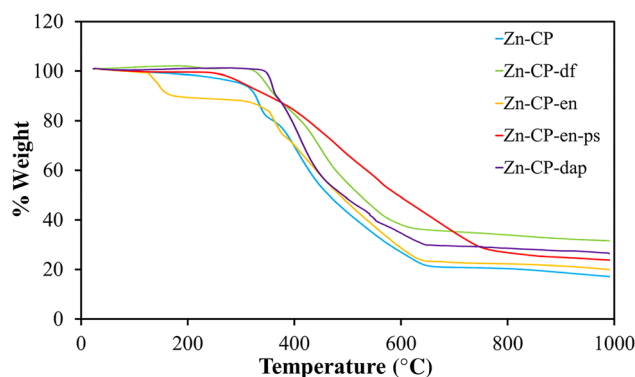**Fig. 11** Zeta potential curves of **Zn-CP** and its PSM derivatives.

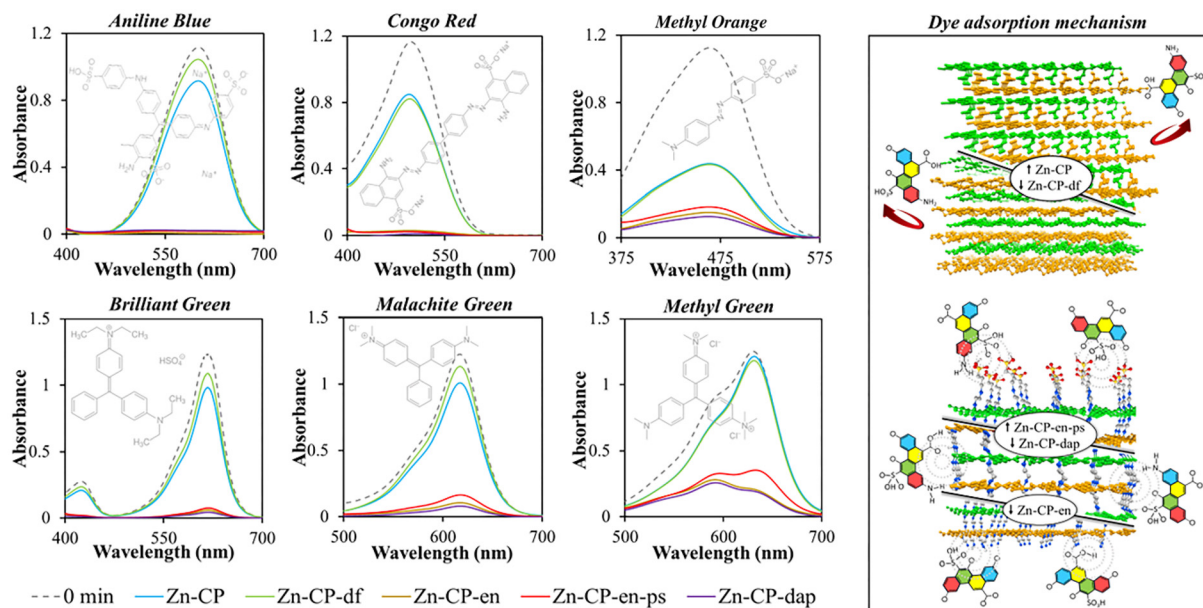**Fig. 12** TGA curves of **Zn-CP** and its PSM derivatives.

Fig. 13 (Left-hand panels) UV-Vis spectra of selected cationic and anionic dyes before and after adsorption by **Zn-CP** and its derivatives in water at equilibrium (180 min). (Right-hand panel) Proposed adsorption mechanism in **Zn-CP** and its derivatives, highlighting active sites for hydrogen bonding with dye molecules (dashed circles).

nation of the compounds. The consistent thermal curve pattern of these compounds suggests that the pristine structure of **Zn-CP** remains intact throughout the PSM process.

Dye adsorption

The designed introduction of functional groups through tandem post-synthetic modification can significantly impact the physicochemical properties of compounds, especially their adsorption behavior. To systematically evaluate the effects of our structural modifications on dye adsorption performance, we have selected Aniline Blue, Methyl Orange, and Congo Red as anionic dyes, and Brilliant Green, Malachite Green, and Methyl Green as cationic dyes to compare the adsorption capabilities of both the parent **Zn-CP** and its modified derivatives. This comparative study enables us to correlate specific functional group modifications with adsorption efficiency, elucidate the roles of Lewis acid and base sites, and examine the influence of Brønsted acid interactions with dye molecules on adsorption efficiency.

Fig. 13 presents the UV-Vis spectral data for the selected cationic and anionic dyes at both 0 minutes and the equilibrium point (180 minutes). The results clearly show that the modified CPs (**Zn-CP-en, Zn-CP-en-ps,** and **Zn-CP-dap**) exhibit superior dye removal efficiency, as evidenced by the dramatic reduction in characteristic dye absorption peaks (λ_{max}) at the equilibrium point compared to the initial spectra. **Zn-CP** and **Zn-CP-df** show limited adsorption capacity, with only low decreases in dye peak intensities. The enhanced performance of the amine-functionalized derivatives (**Zn-CP-en** and **Zn-CP-dap**) suggests that hydrogen bonding between the amine groups and dyes for both dye types remarkably enhances the dye adsorption per-

formance. The effectiveness of **Zn-CP-en-ps** implies synergistic effects from both amine (–NH$_2$) and sulfonate (–SO$_3$H) groups. The limited dye adsorption capacity of **Zn-CP-df** indicates weak interaction between the Zn-AIP network and dye molecules.

Notably, the unmodified **Zn-CP** and **Zn-CP-df** adsorbents, which possess open metal sites, exhibit limited removal efficiency (<35% for most dyes), except for Methyl Orange (~65%) (Table 3). In contrast, the modified adsorbents (**Zn-CP-en, Zn-CP-en-ps,** and **Zn-CP-dap**) achieve exceptional performance, with nearly complete removal of almost all dyes. Additionally, the removal efficiency of Methyl Green improved dramatically from 3.07% (**Zn-CP**) to 81.03% (**Zn-CP-dap**), highlighting the crucial role of surface functionalization. The results suggest that modifications introduced amine or oxygen-rich groups, enhancing interactions with both cationic and anionic dyes. For instance, **Zn-CP-dap** consistently achieved >99% removal for Aniline Blue, Congo Red, and Brilliant Green, outperforming its unmodified counterparts. The stark contrast in performance underscores the importance of chemical tuning for targeted dye adsorption.

Table 3 Dye removal efficiency (%) of **Zn-CP** and its derivatives for the selected cationic and anionic dyes

Dye	Type	Zn-CP	Zn-CP-df	Zn-CP-en	Zn-CP-en-ps	Zn-CP-dap
Aniline Blue	Anionic	18.12	6.75	>99	>99	>99
Congo Red	Anionic	32.59	34.78	>99	>99	>99
Methyl Orange	Anionic	61.87	61.13	83.76	79.03	85.82
Brilliant Green	Cationic	21.91	12.74	>98	>98	>98
Malachite Green	Cationic	17.95	7.64	92.80	89.59	94.97
Methyl Green	Cationic	3.07	5.47	79.88	68.97	81.03

It is well established that dye adsorption mechanisms can involve multiple interactions, including $\pi\cdots\pi$ interactions, hydrogen bonding, cation exchange, pore filling, and electrostatic attraction. Based on our experimental results, it appears that hydrogen bonding is the dominant mechanism in our system, while $\pi\cdots\pi$ stacking and electrostatic interactions contribute to a much lesser extent.[63]

Despite the very high positive zeta potential of **Zn-CP-df**, it showed poor adsorption of both anionic and cationic dyes. This suggests that a strong positive surface charge alone does not guarantee significant dye uptake *via* electrostatic attraction. In contrast, **Zn-CP-en**, **Zn-CP-dap**, and **Zn-CP-en-ps** exhibited efficient adsorption of both anionic and cationic dyes, despite their surface charges ranging from ~+6 to +10 mV. This performance is likely due to the presence of functional groups ($-NH_2$ and $-SO_3H$) that can form strong hydrogen bonds with dye molecules. Therefore, the observed trends can be rationalized by the functionalization-driven enhancement of specific interactions, rather than by surface charge alone. Additionally, in **Zn-CP** and **Zn-CP-df**, the stacked-layer structures likely limit dye accessibility, whereas in the functionalized structures, layer separation facilitates better interaction of dye molecules with the active sites within the frameworks, further promoting dye uptake.

The proposed adsorption mechanism including the active sites responsible for hydrogen bonding is illustrated in Fig. 13.

Conclusion

In this study, we demonstrated a systematic three-step tandem post-synthetic modification (PSM) strategy to enhance the structure and functionality of a 2D layered zinc coordination polymer (**Zn-CP**). Initially, the removal of coordinated DMSO molecules generated **Zn-CP-df** with coordinatively unsaturated Lewis acid sites, followed by exfoliation into nanosheets (**Zn-CP-df-ex**) to increase the accessible surface area. In the second step, ethylenediamine (en) and 1,3-diaminopropane (dap) were introduced to anchor amine functionalities, forming **Zn-CP-en** with a multilayered structure featuring accessible Lewis base sites, and **Zn-CP-dap**, which developed into a 3D supramolecular framework through interlayer cross-linking. Finally, sulfonic acid groups were grafted onto **Zn-CP-en** *via* 1,3-propanesultone, producing **Zn-CP-en-ps** with Brønsted acid character.

These modifications resulted in a dramatic improvement in dye adsorption performance, with **Zn-CP-en**, **Zn-CP-en-ps**, and **Zn-CP-dap** achieving >80% removal efficiency for both cationic and anionic dyes, significantly outperforming the unmodified **Zn-CP**, which exhibited <35% efficiency for most dyes. The enhanced performance is attributed to the synergistic effects of amine and sulfonic acid functionalities, which promote hydrogen bonding with dye molecules.

Overall, this work demonstrates the potential of tandem PSM as a versatile and effective strategy for designing coordination polymers with tailored functionalities, providing prom-

ising avenues for the development of advanced materials for environmental remediation and related applications.

Conflicts of interest

There are no conflicts to declare.

Data availability

The data that support the findings of this study are available from the corresponding author upon reasonable request. The datasets include powder X-ray diffraction (PXRD) patterns, infrared (IR) spectroscopy data, thermogravimetric analysis (TGA) results, zeta potential values, and dye adsorption data. All relevant data are included in the manuscript and its ESI.†

Acknowledgements

References

1 C. Tan, X. Cao, X. J. Wu, Q. He, J. Yang, X. Zhang, J. Chen, W. Zhao, S. Han, G. H. Nam, M. Sindoro and H. Zhang, *Chem. Rev.*, 2017, **117**, 6225–6331.

2 Y. Chen, Z. Fan, Z. Zhang, W. Niu, C. Li, N. Yang, B. Chen and H. Zhang, *Chem. Rev.*, 2018, **118**, 6409–6455.

3 S. Mandal, S. Natarajan, P. Mani and A. Pankajakshan, *Adv. Funct. Mater.*, 2021, **31**, 3751–3891.

4 K. S. Novoselov, A. K. Geim, S. V. Morozov, D. Jiang, Y. Zhang, S. V. Dubonos, I. V. Grigorieva and A. A. Firsov, *Science*, 2004, **306**, 666–669.

5 M. Chhowalla, H. S. Shin, G. Eda, L. J. Li, K. P. Loh and H. Zhang, *Nat. Chem.*, 2013, **5**(4), 263–275.

6 X. Huang, Z. Zeng and H. Zhang, *Chem. Soc. Rev.*, 2013, **42**, 1934–1946.

7 W. J. Ong, L. L. Tan, Y. H. Ng, S. T. Yong and S. P. Chai, *Chem. Rev.*, 2016, **116**, 7159–7329.

8 L. Tao, E. Cinquanta, D. Chiappe, C. Grazianetti, M. Fanciulli, M. Dubey, A. Molle and D. Akinwande, *Nat. Nanotechnol.*, 2015, **10**, 227–231.

9 E. Pomerantseva and Y. Gogotsi, *Nat. Energy*, 2017, **2**, 17089.

10 Y. Peng, Y. Huang, Y. Zhu, B. Chen, L. Wang, Z. Lai, Z. Zhang, M. Zhao, C. Tan, N. Yang, F. Shao, Y. Han and H. Zhang, *J. Am. Chem. Soc.*, 2017, **139**, 8698–8704.

11 M. Zhao, Q. Lu, Q. Ma and H. Zhang, *Small Methods*, 2017, **1**, 1600030.

12 V. K. Maka, A. Mukhopadhyay, G. Savitha and J. N. Moorthy, *Nanoscale*, 2018, **10**, 22389–22399.

13 H. S. Wang, J. Li, J. Y. Li, K. Wang, Y. Ding and X. H. Xia, *NPG Asia Mater.*, 2017, **9**(3), e354.

14 A. Tarassoli, V. Nobakht, E. Baladi, L. Carlucci and D. M. Proserpio, *CrystEngComm*, 2017, **19**, 6116–6126.

15 E. Baladi, V. Nobakht, A. Tarassoli, D. M. Proserpio and L. Carlucci, *Cryst. Growth Des.*, 2018, **18**, 7207–7218.

16 W. Pang, B. Shao, X. Q. Tan, C. Tang, Z. Zhang and J. Huang, *Nanoscale*, 2020, **12**, 3623–3629.

17 P. Daraei, E. Rostami, F. Nasirmanesh and V. Nobakht, *J. Environ. Manage.*, 2023, **347**, 119083.

18 B. Zhou and D. Yan, *Adv. Funct. Mater.*, 2023, **33**, 2300735.

19 Y. L. Liu, X. Y. Liu, L. Feng, L. X. Shao, S. J. Li, J. Tang, H. Cheng, Z. Chen, R. Huang, H. C. Xu and J. L. Zhuang, *ChemSusChem*, 2022, **15**, 202102603.

20 Y. Lin, L. Li, Z. Shi, L. Zhang, K. Li, J. Chen, H. Wang and J. M. Lee, *Small*, 2024, **20**, 2309841.

21 Z.-Q. Shi, N.-N. Ji, M.-H. Wang and G. Li, *Inorg. Chem.*, 2020, **59**, 4781–4789.

22 J. Liu, X. Song, T. Zhang, S. Liu, H. Wen and L. Chen, *Angew. Chem.*, 2021, **133**, 5672–5684.

23 Y. Zhong, X. Xu, W. Wang and Z. Shao, *Batteries Supercaps*, 2019, **2**, 272–289.

24 M. E. Ziebel, C. A. Gaggioli, A. B. Turkiewicz, W. Ryu, L. Gagliardi and J. R. Long, *J. Am. Chem. Soc.*, 2020, **142**, 2653–2664.

25 M. Yao, J. Zheng, A. Wu, G. Xu, S. S. Nagarkar, G. Zhang, M. Tsujimoto, S. Sakaki, S. Horike, K. Otake and S. Kitagawa, *Angew. Chem., Int. Ed.*, 2020, **59**, 172–176.

26 A. Nikseresht, F. Ghoochi and M. Mohammadi, *ACS Omega*, 2024, **9**, 28114–28128.

27 A. D. Burrows, L. C. Fisher, T. J. Mays, S. P. Rigby, S. E. Ashbrook and D. M. Dawson, *J. Organomet. Chem.*, 2015, **792**, 134–138.

28 D. Majumdar, S. Dey, A. Kumari, T. K. Pal, K. Bankura and D. Mishra, *Spectrochim. Acta, Part A*, 2021, **254**, 119612.

29 D. Majumdar, Y. Agrawal, R. Thomas, Z. Ullah, M. K. Santra, S. Das, T. K. Pal, K. Bankura and D. Mishra, *Appl. Organomet. Chem.*, 2020, **34**, 5269.

30 A. Beheshti, W. Clegg, V. Nobakht and R. W. Harrington, *Cryst. Growth Des.*, 2013, **13**, 1023–1032.

31 A. Beheshti, W. Clegg, S. A. Mousavi Fard, R. W. Harrington, V. Nobakht and L. Russo, *Inorg. Chim. Acta*, 2011, **376**, 310–316.

32 S. Azizzadeh, V. Nobakht, L. Carlucci and D. M. Proserpio, *Polyhedron*, 2020, **175**, 114236.

33 V. Nobakht, A. Beheshti, D. M. Proserpio, L. Carlucci and C. T. Abrahams, *Inorg. Chim. Acta*, 2014, **414**, 217–225.

34 A. Beheshti, V. Nobakht, L. Carlucci, D. M. Proserpio and C. Abrahams, *J. Mol. Struct.*, 2013, **1037**, 236–241.

35 S. Mandal, S. Natarajan, P. Mani and A. Pankajakshan, *Adv. Funct. Mater.*, 2021, **31**, 2006291.

36 S. S.-Y. Chui, S. M.-F. Lo, J. P. H. Charmant, A. G. Orpen and I. D. Williams, *Science*, 1999, **283**, 1148–1150.

37 H. Zhang, W. Yu, Y. Lin and G. Jin, *Angew. Chem.*, 2021, **133**, 15594–15599.

38 Z. Sharifzadeh and A. Morsali, *Coord. Chem. Rev.*, 2022, **459**, 214445.

39 C. Yue, L. Wu, Y. Lin, Y. Lu, C. Shang, R. Ma, X. Zhang, X. Wang, W. D. Wu, X. D. Chen and Z. Wu, *ACS Appl. Mater. Interfaces*, 2021, **13**, 26264–26277.

40 M. Kaur, S. Kumar, S. A. Younis, M. Yusuf, J. Lee, S. Weon, K. H. Kim and A. K. Malik, *Chem. Eng. J.*, 2021, **423**, 130230.

41 Z. Wang and S. M. Cohen, *Angew. Chem., Int. Ed.*, 2008, **47**, 4699–4702.

42 Y. Jiang, G. H. Ryu, S. H. Joo, X. Chen, S. H. Lee, X. Chen, M. Huang, X. Wu, D. Luo, Y. Huang, J. H. Lee, B. Wang, X. Zhang, S. K. Kwak, Z. Lee and R. S. Ruoff, *ACS Appl. Mater. Interfaces*, 2017, **9**, 28107–28116.

43 P. Zhou, X. Wang, L. Yue, L. Fan and Y. He, *Inorg. Chem.*, 2021, **60**, 14969–14977.

44 Y.-P. Xia, C.-X. Wang, M.-H. Yu and X.-H. Bu, *Chin. Chem. Lett.*, 2021, **32**, 1153–1156.

45 M. Alizadeh-Bavieh, V. Nobakht, T. Sedaghat, L. Carlucci, P. Mercandelli and M. Taghavi, *J. Solid State Chem.*, 2021, **294**, 121855.

46 Y. Zhang, B. Li, W. Guan, Y. Wei, C. Yan, M. Meng, J. Pan and Y. Yan, *Cellulose*, 2020, **27**, 3037–3054.

47 Z. Weng, T. Yu and F. Zaera, *ACS Catal.*, 2018, **8**, 2870–2879.

48 A. Erxleben, *Coord. Chem. Rev.*, 2003, **246**, 203–228.

49 Y. H. Luo, C. Wang, S. H. Ma, X. W. Jin, Y. C. Zou, K. X. Xu, W. X. Fang, L. Zhang and H. Dong, *Environ. Sci. Nano*, 2021, **8**, 3665–3672.

50 A. K. Singh, A. Yadav, A. Indra and R. B. Rastogi, *Colloids Surf., A*, 2021, **613**, 126100.

51 C. Wang, L. Zhang, J. Y. Wang, S. Su, X. W. Jin, P. J. An, B. W. Sun and Y. H. Luo, *FlatChem*, 2020, **24**, 100193.

52 S. Chakrabarty, S. H. Deshmukh, A. Barman, S. Bagchi and A. Ghosh, *J. Phys. Chem. B*, 2022, **126**, 4501–4508.

53 S. G. Ghomshehzadeh, V. Nobakht, N. Pourreza, P. Mercandelli and L. Carlucci, *Polyhedron*, 2020, **176**, 114265.

54 W. Yang, C. Wang and V. Arrighi, *J. Mater. Sci.: Mater. Electron.*, 2018, **29**, 2771–2783.

55 A. G. Moritz, *Nature*, 1962, **195**, 800.

56 K. I. Oh and C. R. Baiz, *J. Chem. Phys.*, 2019, **151**, 234107.

57 C. De Wu, C. Z. Lu, W. B. Yang, H. H. Zhuang and J. S. Huang, *Inorg. Chem.*, 2002, **41**, 3302–3307.

58 K. O. Kongshaug and H. Fjellvåg, *Inorg. Chem.*, 2006, **45**, 2424–2429.

59 S. Y. Yang, H. B. Yuan, X. B. Xu and R. B. Huang, *Inorg. Chim. Acta*, 2013, **403**, 53–62.

60 M. A. LeRoy, A. S. Perera, S. Lamichhane, A. N. Mapile, F. Khaliq, K. Kadota, X. Zhang, S. Ha, R. Fisher, D. Wu, C. Risko and C. K. Brozek, *Chem. Mater.*, 2024, **36**, 3673–3682.

61 A. N. Mapile, M. A. LeRoy, K. Fabrizio, L. F. Scatena and C. K. Brozek, *ACS Nano*, 2024, **18**, 13406–13414.

62 Y. Guo, Y. Ying, Y. Mao, X. Peng and B. Chen, *Angew. Chem.*, 2016, **128**, 15344–15348.

63 M. S. Khan, M. Khalid and M. Shahid, *Mater. Adv.*, 2020, **1**, 1575–1601.